

See discussions, stats, and author profiles for this publication at: <https://www.researchgate.net/publication/296196752>

# Physical and Numerical Modeling of Unsteady Cavitation Dynamics

Conference Paper · May 2001

---

CITATIONS

145

READS

2,603

**1 author:**



Günter H. Schnerr Professor Dr.-Ing.habil.

Technische Universität München

147 PUBLICATIONS 1,303 CITATIONS

[SEE PROFILE](#)

**Some of the authors of this publication are also working on these related projects:**



Cavitation - Physical and numerical modeling based on bubble dynamics [View project](#)

# Physical and Numerical Modeling of Unsteady Cavitation Dynamics

Günter H. Schnerr, Jürgen Sauer  
University of Karlsruhe  
Kaiserstr. 12, 76128 Karlsruhe, Germany  
e-mail: guenter.schnerr@mach.uni-karlsruhe.de

## Abstract

Herein we present the actual status of our physical and numerical modeling of dispersed unsteady cavitating flows for large scale hydrodynamic turbomachinery. The cavitation model allows simultaneous application of standard VOF techniques, together with our newly developed dispersed VOF method for predicting growth and collapse of bubble clouds, which calculates the time dependent vapor distribution within each computational cell. Extensive tests have been performed to demonstrate quantitatively discretization effects of the numerical method and scaling effects of the cavitation model. The present model neglects the viscosity of the fluid to demonstrate and to resolve large and small scale phenomena of developed unsteady cavitation dynamics with the periodic formation of re-entry jets, shedding and collapse of bubble clouds and the resulting hydrodynamic pressure waves. Simulations of internal flows through nozzles and of external flows over NACA 0015 hydrofoils demonstrate the sensitivity of the results against the reference location of the pressure boundary conditions and of the damping effect of free surfaces.

## 1. Introduction

Cavitation occurs in flows of liquids when the local static pressure falls below the vapor pressure, resulting in regions of vapor. It can occur in a broad variety of technical devices where it usually degrades their performance, accompanied with intense erosion of structural components and very loud noise, see e.g. the review by Arndt (1981). It is interesting to note that cavitation can also be found in nature, e.g. snapping shrimps produce a loud snapping sound by an extremely fast closure of their snappers which produce a high speed collapsing jet to kill prey animals (e.g. Versluis et al., 2000).

Progress in understanding of cavitation phenomena is of great importance and interest for industry. In the past, several models were developed to simulate cavitation (e.g. Schnerr et al., 1995, Reboud & Delannoy, 1994), which do in general not model the complicated and highly transient bubble growth and collapse. This process is responsible for the cavitation damage and therefore, the location where the bubbles collapse is of great interest and the need for a cavitation model rises that also includes effects based on bubble dynamics. Since hydrofoils make up so many different types of machines - pumps, turbines, propellers- the study of how cavitation affects hydrofoil performance is of special interest.

The type of cavitation most frequently observed at hydrofoils with a well-rounded leading edge is the so-called traveling bubble cavitation. From experiments it can be seen that for such foils the cavitation region is made up of individual bubbles rather than by a large vapor-filled cavity. These bubbles originate from small cavitation nuclei (particles, air bubbles), which are already existing in the bulk flow. The nuclei reach the low pressure region (suction peak) and grow to vapor bubbles while they are convected downstream, supposed the static pressure is sufficiently below the vapor pressure. Then, the bubbles are swept in the region of higher pressure and finally collapse. Many experimental studies, see e.g. Gindroz (1976), Keller (1999) and Li & Ceccio (1994), point out the importance of the nuclei content of the liquid for the inception and development of cavitation. The nuclei content affects the tensile strength of the liquid and therefore is responsible if or if not cavitation occurs at given conditions.

At the beginning clouds form a dispersed sheet attached to the solid surface, which seems to be steady at first sight. Due to the entrainment of bubbles into the wake the sheet becomes unstable, causing large parts of the cavity to break off. The resulting dynamics forms by interaction between the dynamics of individual bubbles and the motion of the liquid fluid. During collapse single bubbles near solid walls create extremely high pressure pulses which seem to be responsible for erosion and destruction, and by global (hydrodynamic) pressure waves, formed during the collapse of bubble clouds (e.g. Brennen, 1998). The aim of the present approach is to improve understanding of the global pressure dynamics, which is not controlled by the viscosity of the fluid.

## 2. Modeling

### 2.1. Physical modeling

Our cavitation model bases on the following physical assumptions: Cavitation is modeled as the growth and collapse process of vapor bubbles. The bubbles originate from nuclei which already exist in the bulk flow and grow or collapse depending on the surrounding conditions (pressure and temperature). It is assumed, that the slip between the vapor bubbles and the liquid can be neglected. The growth of vapor bubbles due to pseudo or gaseous cavitation is not yet taken into account. Cavitation is assumed to be dominated by heterogeneous nucleation, hence a homogeneous nucleation theory, known e.g. from modeling of condensing flows is not employed. The interested reader may refer to see Winkler, Heiler and Schnerr (1999).

The perhaps most important feature of the model is, that it resolves the interior dispersed structure of the bubble cloud. From a numerical point of view, the cavitation model calculates the production (bubble growth), destruction (bubble collapse) and convection of the vapor phase. But due to the underlying modeling of the nuclei content, it is possible to reconstruct from the vapor content of the cell, the number of bubbles that are currently in the cell and their radii. Therefore, a certain value of the vapor fraction  $\alpha$  directly corresponds to a certain bubble radius  $R$ . Radius and vapor fraction are related by Eq. 5.

### 2.2. Numerical modeling

The occurrence of cavitation leads to a two-phase flow with phase transition. Entering or leaving the cavitation region, the mixture density jumps from the pure liquid to a much smaller value or vice versa.

To overcome problems due to a discontinuous density distribution, a special numerical treatment is required. Front tracking methods (level set, marker particles, surface-fitting) were not found to be suitable since they require the presence of distinct interfaces to be tracked. In this context, here the interface is simply the bubble wall, that separates the vapor from the liquid phase. Because of the huge number of bubbles (typically 1000 per  $cm^3$  liquid) and consequently a huge number of interfaces to be tracked, the usage of interface tracking methods would result in enormous CPU time and storage requirements. Instead, we prefer the usage of a front capturing method, namely the Volume-of-Fluid technique, proposed by Nichols & Hirt (1973). For a detailed description of the numerical treatment see Sauer (2000).

### 2.3. Modified Volume-of-Fluid method for simulation of cavitation clouds

The Volume-of-Fluid (VOF) method tracks the motion of a certain fluid volume through the computational domain, irrespective whether the volume contains pure liquid, pure vapor or a mixture of vapor bubbles and liquid. Within the scope of the VOF approach, the two-phase flow is treated as a homogeneous mixture and hence only one set of equations is used for description. The VOF method requires in addition to the continuity and the momentum equations (which are coupled by a SIMPLE algorithm), the solution of a transport equation for the cell vapor fraction  $\alpha$ , which is defined as the ratio of the vapor (gas) volume to the cell volume, see Eq. 5:

$$\frac{\partial \alpha}{\partial t} + \frac{\partial(\alpha u)}{\partial x} + \frac{\partial(\alpha v)}{\partial y} = 0, \quad (1)$$

where  $u$  and  $v$  are Cartesian components of the velocity vector  $\mathbf{u}$ . The equations of motion are closed with the constitutive relations for the density and dynamic viscosity:

$$\varrho = \alpha \varrho_v + (1 - \alpha) \varrho_l, \quad (2)$$

$$\mu = \alpha \mu_v + (1 - \alpha) \mu_l. \quad (3)$$

Here the subscripts  $l$  and  $v$  stand for the properties of pure liquid and pure vapor which are assumed to be constant. The equations derived are general and describe the motion of two fluids with an interface between them. A more detailed discussion of the governing equations without phase transition can be found for example in the work of Ubbink (1997). As suggested by Spalding (1974), the continuity equation is used in its non-conservative form:

$$\nabla \cdot \mathbf{u} = -\frac{1}{\varrho} \frac{d\varrho}{dt}. \quad (4)$$

The usage of the volume fluxes rather than mass fluxes (conservative form) accounts for the numerical advantage that the volume fluxes are continuous at the interfaces and thus simplifies the solution of the pressure correction equation. For standard VOF applications, i.e. both fluids are assumed to be incompressible and no phase transition takes place, the rhs. of Eq. 4 reduces to zero, meaning that the flow field is divergence-free. Care has to be taken for discretisation of the volume fraction Eq. 1. In order to avoid smearing of the interface, special methods are used to derive the cell face values for the void fraction  $\alpha$ . For that reason, the CICSAM-Scheme (Compressive Interface Capturing on Arbitrary Meshes) as proposed by Ubbink (1997) was implemented and the code was verified by several test cases (convection tests, sloshing, dam breaking). Note that the CICSAM scheme is employed, if there exists a discrete sharp interface to be tracked, e.g. the motion of the free surface, see Sauer (2000). In the case of cavitation, the vapor bubbles and hence the vapor fraction are homogenously distributed in the computational cell. A schematic sketch of the distribution of the gaseous phase for a standard VOF-application and for cavitation is presented in Fig. 1 to explain this difference.

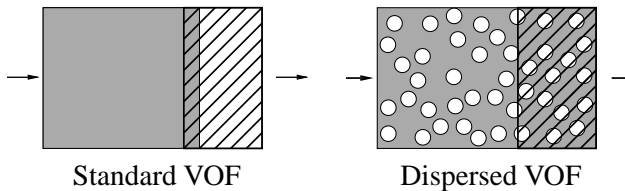


Fig. 1: Distribution of the gaseous phase in a computational cell. Left: Standard VOF application, non-homogeneous distribution. Right: Cavitation, homogeneous distribution of the gaseous phase within the liquid. The marked volume leaves the cell due to convection.

In contrast to standard VOF applications, cavitation leads to a polydispersed two-phase flow including phase transition. The bubbles grow and collapse and hence change the vapor fraction in a computational cell, in addition to the convective transport. The standard VOF method does account for convective transport, but not for phase transition. With respect to cavitation, the void fraction  $\alpha$  may be reformulated as follows:

$$\alpha = \frac{V_v}{V_{cell}} = \frac{N_{bubbles} \cdot \frac{4}{3}\pi R^3}{V_v + V_l} = \frac{n_0 V_l \cdot \frac{4}{3}\pi R^3}{n_0 V_l \cdot \frac{4}{3}\pi R^3 + V_l} = \frac{n_0 \cdot \frac{4}{3}\pi R^3}{1 + n_0 \cdot \frac{4}{3}\pi R^3}, \quad (5)$$

where  $V_{cell}$  is the volume of the computational cell,  $V_v$  and  $V_l$  are the volumes occupied by vapor and liquid, respectively and  $N_{bubbles}$  is the number of bubbles in the computational cell. As a consequence of the bubble growth process, the velocity field is no longer divergence-free (Eq. 6) and the void fraction (Eq. 7) has to be extended by a vapor production source term:

$$\nabla \cdot \mathbf{u} = -\frac{\varrho_v - \varrho_l}{\alpha \varrho_v + (1 - \alpha) \varrho_l} \frac{d\alpha}{dt}, \quad (6)$$

$$\frac{\partial \alpha}{\partial t} + \frac{\partial(\alpha u)}{\partial x} + \frac{\partial(\alpha v)}{\partial y} = \left( \frac{n_0}{1 + n_0 \cdot \frac{4}{3}\pi R^3} \right) \frac{d}{dt} \left( \frac{4}{3}\pi R^3 \right). \quad (7)$$

The vapor production is taken into account by the source term on the right hand side of Eq. 7. The change of the cell vapor fraction does now depend on the number of bubbles per cell volume (rhs:1st term) times the volume change of a single bubble (rhs:2nd term) and the convective transport. The parameter  $n_0$  is defined as the bubble concentration per unit volume of pure liquid. Using this definition, the number of nuclei is explicitly coupled to the water volume in a cell. The physical background of this more formal aspect is, that relating the number of bubbles to the water volume (rather than to the volume of the mixture) guarantees the conservation of the number of bubbles. If the nuclei grow, the vapor fraction rises and hence the water fraction decreases. Therefore, the number of bubbles in the cell does also decrease. In Fig. 2 the growth of nuclei in a cell is schematically depicted. For the initial situation, Fig. 2 left, the cell contains a large water fraction and hence a large number of nuclei. If

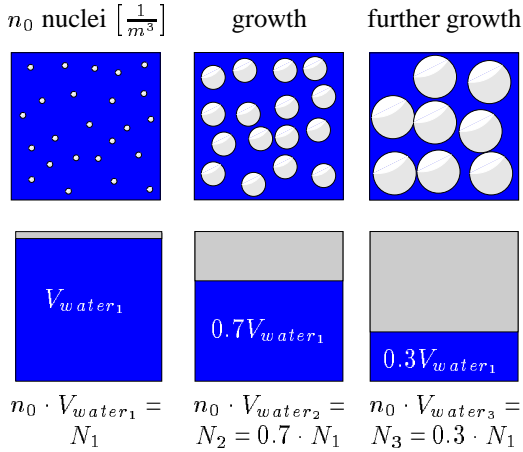


Fig. 2: Number of bubbles depending on the water fraction in a computational cell. Left: Initial simulation. Middle: Growth of the nuclei. Right: Further growth of the vapor bubbles.

the nuclei grow, Fig. 2 middle, they displace water and at the same time other bubbles. Therefore, the gain of vapor fraction due to nuclei growth is reduced by a loss of vapor fraction due to bubbles that are displaced out of the cell. Further growth, Fig. 2 right, leads to a further reduction of the number of bubbles. Since every vapor bubble originates from a nuclei, the definition of  $n_o$  also holds for vapor bubbles. A given volume of water  $V_l$  always contains  $N = n_o \cdot V_l$  bubbles, the bubbles can either be nuclei of radius  $R = R_0$  or vapor bubbles with arbitrary radius. The interested reader may refer to Sauer (2000) for further explanation of modeling the nuclei content of the flow.

Note that for the discretisation of the convection terms of Eq. 7 the UPWIND differencing scheme of Ferziger and Perić (1996) is employed. This is consistent with the homogeneous assumption. A mixture of liquid and bubbles leaves the cell, as shown in Fig. 1. The composition of the fluid volume that is convected out of the cell has the same composition than the fluid that is currently in that cell. This physical aspect is numerically taken into account by using UPWIND discretisation.

To complete the derivation of the numerical method, a relation to model the bubble growth is needed. Under the assumptions that bubble-bubble interactions and bubble coalescence can be neglected and that the bubbles remain spherical, the Rayleigh-Plesset equation, see Plesset (1977), together with the energy equation is well suited to model the bubble growth and collapse process:

$$R \frac{d^2 R}{dt^2} + \frac{3}{2} \left( \frac{dR}{dt} \right)^2 = \frac{p(R) - p_\infty}{\rho_l} - \frac{2\sigma}{\rho_l R} - 4 \frac{\mu}{\rho_l R} \frac{dR}{dt}. \quad (8)$$

Note that in our model the Rayleigh-Plesset equation can be treated as an ordinary differential equation, even when dealing with 2-D or 3-D flow problems, and can e.g. be solved by a Runge - Kutta method. For details of the solution procedure we refer to the work of Lee et al. (1996).

If the system pressure is sufficiently low and the pressure difference  $p(R) - p_\infty$  is large, the Rayleigh relation (9) may be considered as an adequate description for the so-called inertia controlled bubble growth:

$$\dot{R} = \sqrt{\frac{2}{3} \frac{p(R) - p_\infty}{\rho_l}}, \quad (9)$$

where  $p(R)$  is the pressure in the liquid at the bubble boundary and  $p_\infty$  is the pressure in the liquid at a large distance from the bubble. Within the scope of this model,  $p(R)$  is set equal to the vapor pressure  $p_{sat}$  and  $p_\infty$  to the ambient cell pressure. The Rayleigh relation was used to obtain the results presented in the following sections. To simulate cavitation in liquids others than cold water, i.e. if thermal effects are important (organic fluids, hot water), the model is extended by a simplified equation for the mixture enthalpy  $h$  to account for the temperature change of the mixture caused by cavitation. For details and results see Sauer and Schnerr (2000). The advantage of the present modeling is the option for simultaneous application of both methods, the standard front capturing method without phase transition and the modified VOF technique to track dispersed voids. Numerical simulations of unsteady cloud cavitation including free surface effects (see chapter 3.2.2) are interesting examples for simultaneous application of these two methods.

### 3. Numerical results

#### 3.1. Unsteady cavitating nozzle flow

First the cavitation model is applied to simulate steady and unsteady cavitating nozzle flows. The geometry and boundary conditions of the 2-D plane nozzle are depicted in Fig. 3. The working fluid is cold water at a constant temperature of  $T = 293.15\text{K}$ . It is well known that under these conditions thermal effects are quantitatively not important. Both phases are assumed to inviscid, compressibility is only taken into account for mixtures if  $0 < \alpha < 1$ . The nuclei concentration  $n_0$  is set to  $10^8 \text{nuclei/m}^3$  water, the vapor fraction at the nozzle inlet  $a_0 = 10^{-5}$ , which corresponds to a nucleus radius of  $30\mu\text{m}$ . The diffuser part downstream of the throat forces all bubbles to collapse inside the nozzle which prevents additional complications at the outflow boundary. As boundary conditions of the reference case we prescribe the velocity at the inlet  $U_{ref} = 10\text{m/s}$  and a constant value of the normalized static pressure at the exit  $\sigma_{exit} = 5.45$ , the reference length  $L_{ref} = 0.1\text{m}$ . To reduce the computational time, we assume symmetry with respect to the nozzle axis. Therefore, only the lower half of the symmetric nozzle is calculated. The reference grid consists of  $58 \times 16$  cells.

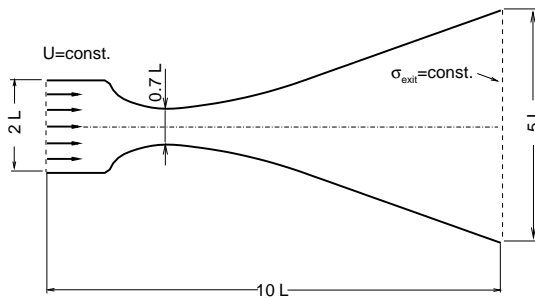


Fig. 3: Geometrical setup of the investigated nozzle,  

$$\sigma_{exit} = \frac{p_{exit} - p_v}{\frac{1}{2} \rho_l U_{ref}^2}.$$

##### 3.1.1. Discretization

Extensive numerical tests have been performed to identify the limit between the steady and unsteady cavitating flow regime. Herein we concentrate on the more relevant unsteady cavitating flows. Figure 4 shows the time dependent total vapor fraction  $\alpha_{total}$  (the integral value of the instantaneous local vapor fraction  $\alpha$  in the computational domain) dependent on the numerical time step, based on the single phase CFL numbers. Obviously, for  $\text{CFL} < 0.1$  the solutions are in good agreement, including the resolution of the secondary peak which represents the instantaneous formation of a bubble cloud. For  $\text{CFL} > 0.1$  this important detail is no more resolved. Figure 4 shows also clearly that after initialisation periodicity establishes after the second cycle, the corresponding oscillation frequency  $f = 9.49\text{Hz}$ .

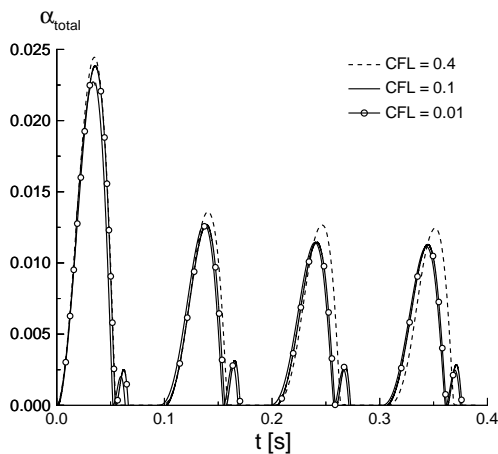


Fig. 4: Influence of CFL number. Total vapor fraction in the nozzle vs. time.  $\sigma_{exit} = 5.45$ ,  $U_{ref} = 10\text{m/s}$ ,  $L_{ref} = 0.1\text{m}$ ,  $n_{0,ref} = 10^8 \text{nuclei/m}^3$  water,  $R_{0,ref} = 3 \cdot 10^{-5}\text{m}$ , water at  $293.15\text{K}$ .

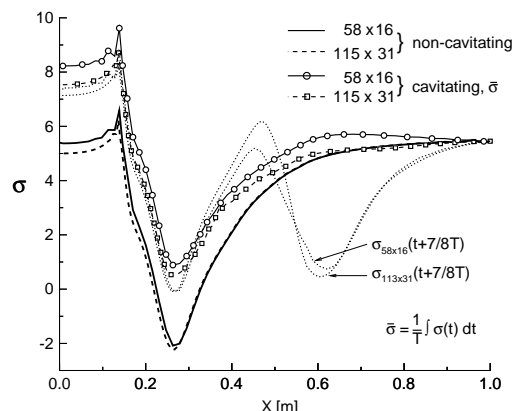


Fig. 5: Mesh effect. Comparison of the  $\sigma$ -distributions at the nozzle wall for different meshes. Dotted: instantaneous  $\sigma$ -distribution.  $\sigma_{exit} = 5.45$ ,  $U_{ref} = 10\text{m/s}$ ,  $L_{ref} = 0.1\text{m}$ ,  $n_{0,ref} = 10^8 \text{nuclei/m}^3$  water,  $R_{0,ref} = 3 \cdot 10^{-5}\text{m}$ , water at  $293.15\text{K}$ .

To check the influence of the spatial discretization we compare results obtained with double resolution, i.e. with  $115 \times 31$  cells, with the reference case. Results for the instantaneous and time averaged  $\sigma$ -distribution along the lower nozzle wall are depicted in Fig. 5. It is interesting to note that the existing differences vary depending on the location in the nozzle. In the throat region the deviations are much lower than at positions downstream. Quantitatively the relative difference shown here disappears immediately for stream lines apart from the nozzle wall, especially along the center line.

### 3.1.2. Scaling effect

An important aspect of the design of hydraulic machinery concerns scaling effects, i.e. effects which cannot be scaled up or down accordingly to classical similarity laws. From extensive experiments of Keller (2000) it is well known, that the development of cavitation depends on the length and velocity scale of the flow field, even if the normalized parameters are kept constant. Reduction of the reference length by one order of magnitude reproduces in tendency what is known from experiments of Keller. In the larger nozzle locally more vapor is formed and the shedding frequency is lower, see Fig. 6. Note that in Fig. 6 the total vapor fraction  $\alpha_{total}$  is plotted against the normalized time  $t^*$  and reduction of the length scale of one order increases the oscillation frequency from  $f = 9.49\text{Hz}$  to  $f = 83.52\text{Hz}$ . From the simplified bubble dynamics Eq. 9 it follows immediately that the present model cannot reveal velocity scale effects.

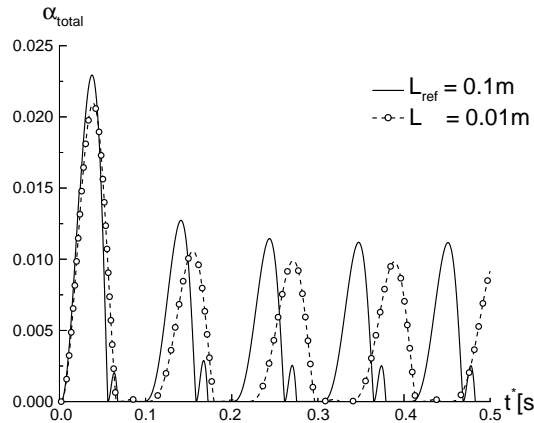


Fig. 6: Length scale effect. Total vapor fraction in the nozzle vs. time.  $t^* = L_{ref}/L \cdot t$ ,  $\sigma_{exit} = 5.45$ ,  $U_{ref} = 10\text{m/s}$ ,  $n_{0,ref} = 10^8\text{nuclei/m}^3\text{water}$ ,  $R_{0,ref} = 3 \cdot 10^{-5}\text{m}$ , water at 293.15K.

### 3.1.3. Variation of cavitation number $\sigma_{ref}$

In the following we investigate the influence of the cavitation number  $\sigma_{exit}$  in the smaller nozzle with  $L_{ref} = 0.01\text{m}$ . Above  $\sigma_{exit} = 6.87$  no cavitation occurs. If the exit pressure starts to decrease we observe small attached vapor sheets with low amplitude oscillations. With further decrease of  $\sigma_{exit}$  the unsteady vapor region growth with increasing frequency toward the nozzle exit (Fig. 7). Figure 8 shows the variation of the frequency and of the maximum of the local vapor fraction  $\alpha_{max}$  against the exit boundary condition  $\sigma_{exit}$ . Near  $\sigma_{exit} = 2$  the frequency reaches a maximum of about 100Hz, then it starts to decrease before the flow turns into steady supercavitating state.

Up to now the constant pressure boundary condition was prescribed at the nozzle exit. Figure 9 shows a simplified model to demonstrate the result of this assumption on the pressure gradient and on the cavitation number after instantaneous formation of a certain vapor volume in the throat region. If the pressure is kept constant at the nozzle exit the displacement of the local vapor volume forces the pressure to increase ahead which tends to weaken and to diminish the vaporization itself. If  $\sigma_{ref}$  is fixed at the nozzle inlet the opposite tendency occurs and the cavitation process will be intensified. In practice the pressure will be affected at both sides, i.e. the inflow and the outflow of the test section will be affected simultaneously.

## 3.2. Unsteady cavitating flow over NACA 0015 hydrofoil

The layout of the 2-D plane test section used by Keller & Arndt (1999) for investigation of the unsteady cavitating flow over a NACA 0015 hydrofoil is shown in Fig. 10. For comparison with our numerical simulation the experiment defined by an inlet velocity  $U=12\text{m/s}$ ,  $\sigma_{ref} = 1.0$  and an angle of attack

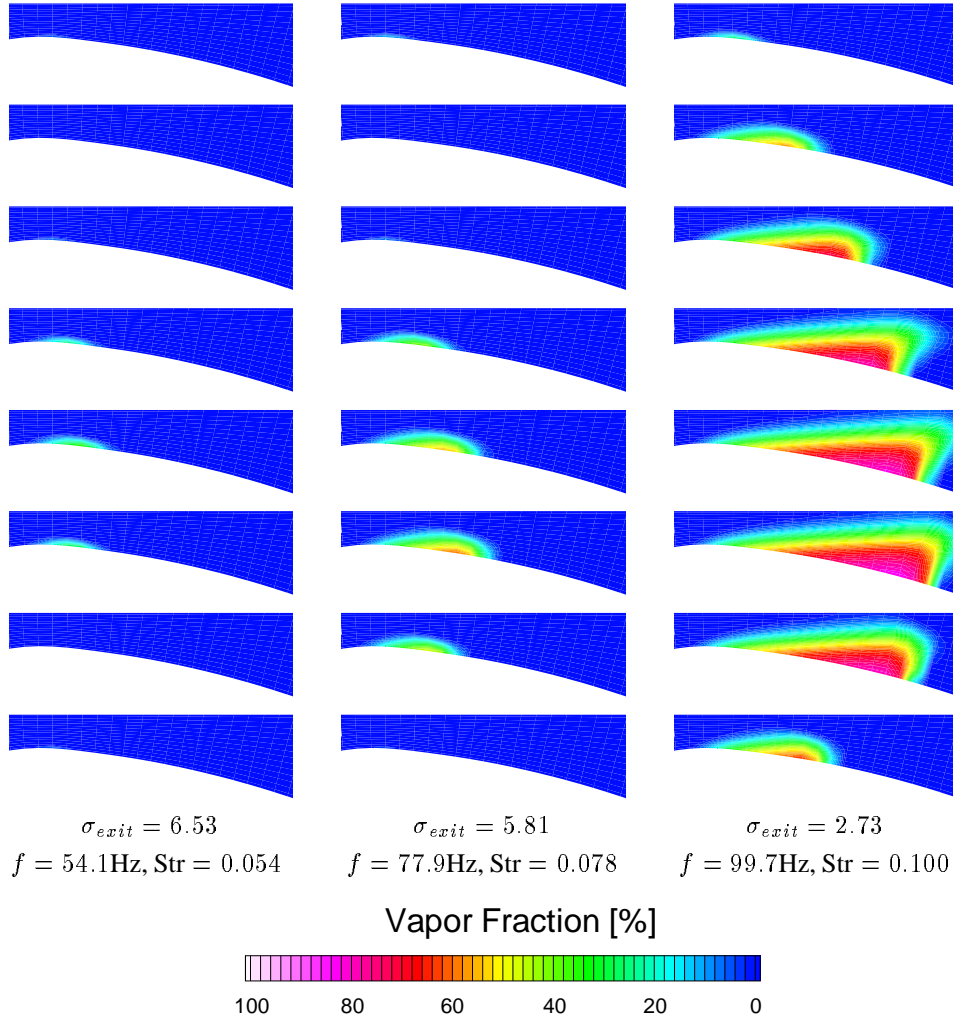


Fig. 7: Variation of cavitation number  $\sigma_{exit}$  at nozzle exit. Vapor fraction distribution, time increment  $\Delta t = T_{period}/8$ .  $U_{ref} = 10\text{m/s}$ ,  $L = 0.01\text{m}$ ,  $n_{0,ref} = 10^8\text{nuclei/m}^3$  water,  $R_{0,ref} = 3.0 \cdot 10^{-5}\text{m}$ , water at 293.15K.

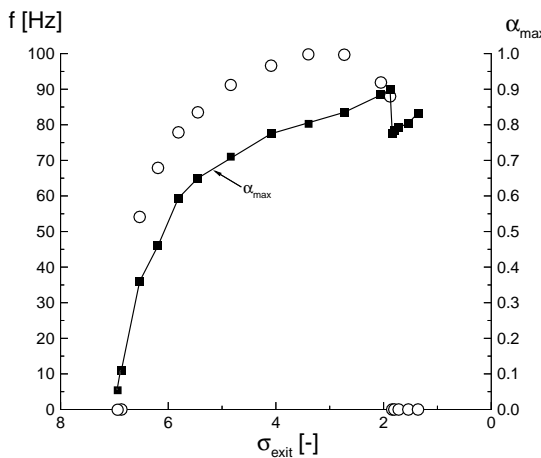


Fig. 8: Effect of cavitation number  $\sigma_{exit}$  at nozzle exit on the frequency and the maximum vapor fraction.  $U_{ref} = 10\text{m/s}$ ,  $L = 0.01\text{m}$ ,  $n_{0,ref} = 10^8\text{nuclei/m}^3$  water,  $R_{0,ref} = 3.0 \cdot 10^{-5}\text{m}$ , water at 293.15K.

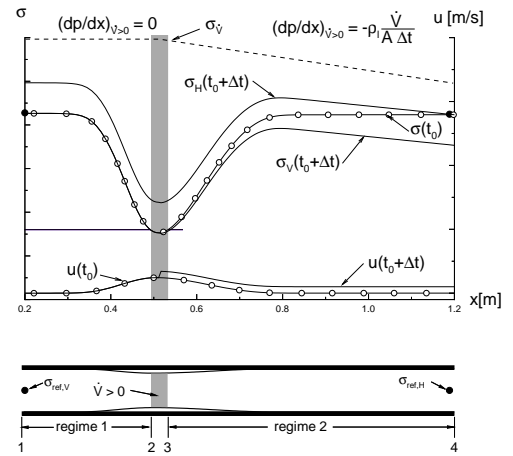


Fig. 9: Inviscid planar channel flow with volume source. Distribution of the pressure and the velocity along the axis before initiating the volume source ( $t = t_0$ ) and thereafter, depending on the position of the reference pressure point. Dashed line: additional pressure gradient owing to volume source.

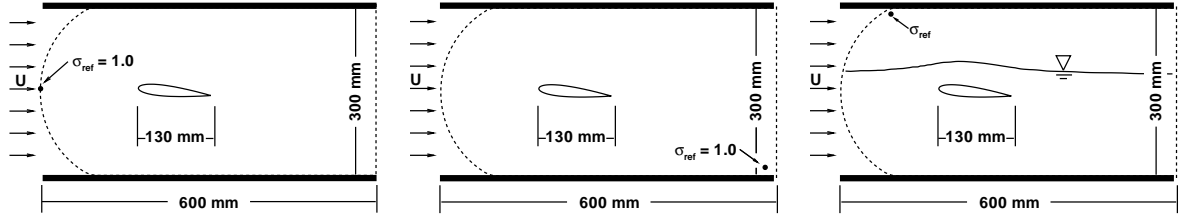


Fig. 10: Geometry and boundary conditions for simulation of cavitating flows. NACA 0015 hydrofoil,  $U = 12\text{m/s}$ ,  $l_c = 0.13\text{m}$ ,  $\alpha_A = 6^\circ$ . Left:  $\sigma$ -reference location upstream of hydrofoil. Middle:  $\sigma$ -reference location downstream. Right:  $\sigma$ -reference location upstream, above the free surface.

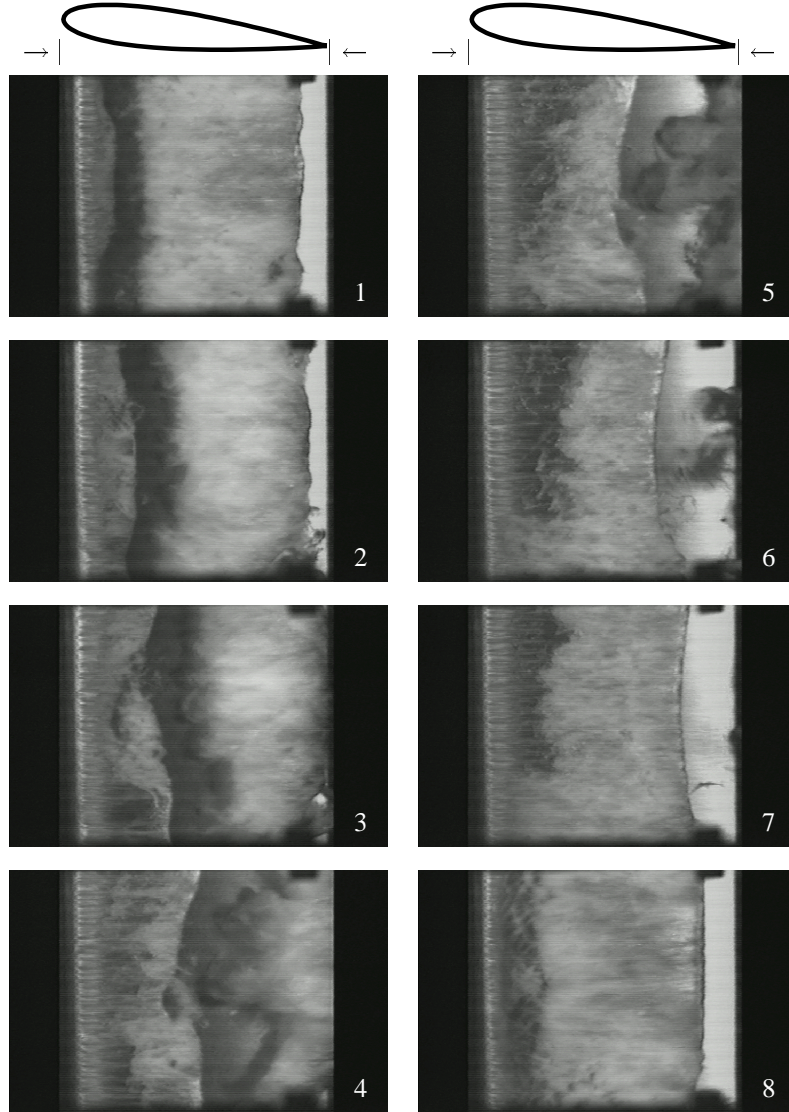


Fig. 11: Cavitation at a NACA 0015 hydrofoil, flow from left, view from above on suction side. Time increment of the photographs:  $\Delta T/8$ .  $f_{\text{exp}} \sim 16\text{Hz}$ ,  $\sigma_{ref} = 1.0$ ,  $U = 12\text{m/s}$ ,  $L_c = 0.13\text{m}$ , cold water; experiment of Keller and Arndt (1999).

$\alpha_A = 6^\circ$  was chosen, because under these conditions in good approximation a 2-D periodic unsteady cavitating flow was observed. Figure 10 also includes different modifications concerning the numerical pressure boundary condition, which are investigated in the following chapter. Figure 11 depicts one cycle of the observed cavitation, the frequency  $f \sim 16\text{Hz}$ , the flow direction is from left to right, the line of sight is on the suction surface, the time marches from the upper left to the lower right picture.

Picture 1: Cavitation starts at the leading edge of the foil and an attached cavity grows. A second

cavitation area exists which originates from the previous cavitation cycle. Pic. 2: The first cavity grows further and the second one is convected downstream. The picture implies that there is a vortex existent, meaning that the water flows upwards in the middle of the foil, flows over the second cavitation area and then flows downwards at the trailing edge. Here, the numerical simulation yields a vortex at the upper side of the foil, see Fig. 12. The vortex rotates clockwise, the experiment (Pic. 3) also implies this direction. Pics. 4 and 5: The formation of a jet is visible which re-enters the cavity. The secondary cavitation region collapses. The primary cavity still grows and reaches its maximum length, Pic. 7. The re-entrant jet reaches the leading edge and breaks off the cavity. The first part collapses, the second one is convected downstream and the cavitation cycle starts again.

### 3.2.1. Variation of location of $\sigma_{ref}$ - Without free surface

The numerical simulation bases on the following additional assumptions: The fluid is cold water at 295.15K with a nuclei concentration  $n_0 = 10^8 \frac{\text{nuclei}}{\text{m}^3 \text{water}}$  and a nuclei radius  $R_0 = 3 \cdot 10^{-5} \text{m}$  in order to match the experimental conditions. The inlet velocity  $U$  is set to 12m/s, the mixture is assumed to be inviscid. The cavitation number is set constant to  $\sigma_{ref} = 1.0$  at the reference point, located 1.5 chord length upstream of the leading edge, see Fig. 10 left.

The series of instantaneous pictures presented in Fig. 12 shows the vapor fraction distribution during

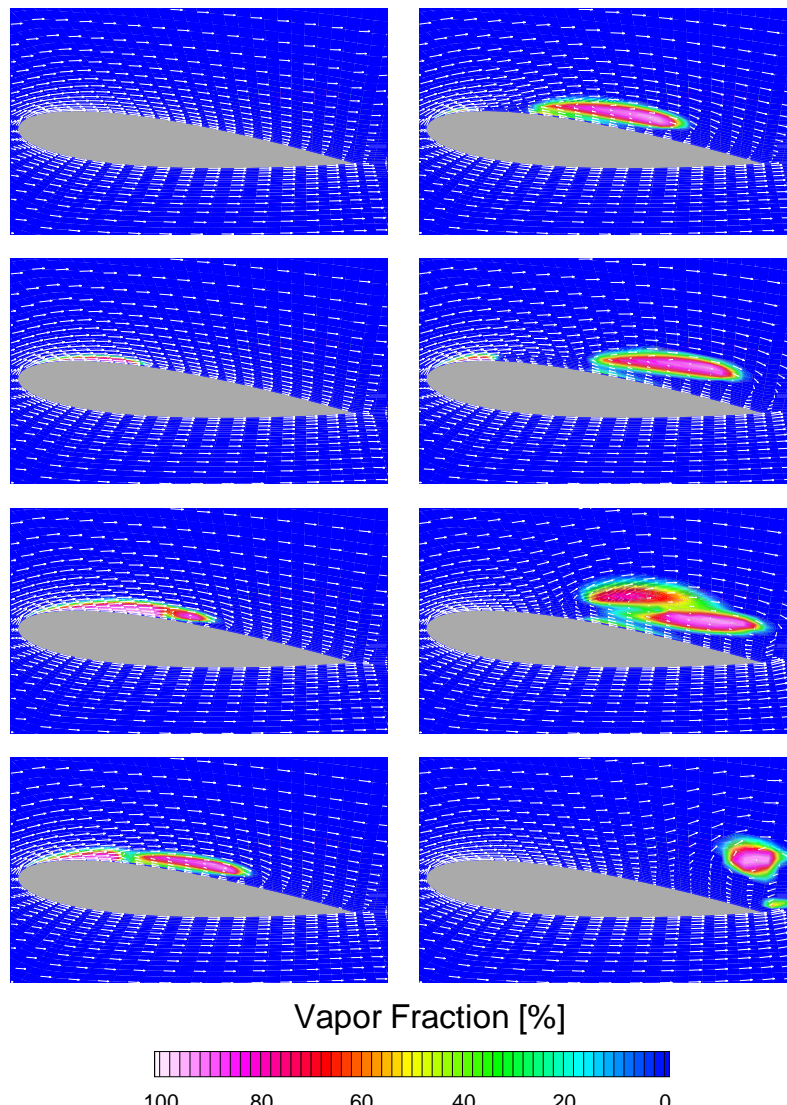


Fig. 12: One cycle of the periodic unsteady cavitating flow over a NACA 0015 hydrofoil. Vapor fraction distribution and velocity vectors. Time increment  $\Delta t = T/8$ ,  $f \approx 11\text{Hz}$ ,  $L_c = 0.13\text{m}$ ,  $\sigma_{ref} = 1.0$ ,  $U = 12\text{m/s}$ ,  $n_{0,ref} = 10^8 \text{nuclei/m}^3$ ,  $R_{0,ref} = 3.0 \cdot 10^{-5} \text{m}$ , water 293.15K, **reference point ahead hydrofoil**.

one cycle of the periodic formation and destruction of the vapor phase. The computed frequency is  $f \approx 10.94\text{Hz}$ , the time increment is  $\Delta t = 0.011\text{s}$ . The vapor cavity starts growing at the leading edge and grows until a re-entrant jets forms and breaks off a part of the cavity (Pics. 1-3). The first part starts to collapse (Pic. 4) and the second part of the cavity is swept downstream. A secondary vapor region forms (Pic. 6), merges with the already existing vapor cloud and finally collapses. The growth and collapse of the vapor phase do significantly alter the pressure distribution and thus change the lift and drag of the hydrofoil. The single phase calculation yields a lift of  $L = 7300\text{N}$  per meter span and a drag of  $D \sim 0$  (inviscid calculation), compared to a time averaged lift of  $L_c = 4200\text{N}$  and drag of  $D_c = 750\text{N}$  under cavitating conditions. Due to cavitation, the lift of the hydrofoil has been substantially decreased (drag increased) which is in agreement with experimental observations of Keller & Arndt (1999).

Figure 12 also illustrates the important effect on the lift which varies to about 100% within one cycle and may even become negative after the collapse of the dispersed vapor cloud near the trailing edge. Frequency and quantitative change of the lift up to 100% are in good agreement with the experiment.

Since the nuclei content of the flow is approximated by an average radius and an average nuclei concentration, parameter variations have been performed to investigate the effect of the nuclei content on the time averaged lift and drag. The simulations show, that lift and drag are rather insensitive to a variation of the number of nuclei, although the time dependent vapor fraction distribution is quite different for the  $n_0$  variations performed. The common fact of all simulations is, that there is one large vortex created which is convected downstream at the suction side of the hydrofoil. This vortex controls the pressure distribution and hence affects lift and drag. The amount of vapor that is present during one cycle is not very significant for lift and drag.

To demonstrate the importance of the a priori not well defined boundary conditions, especially of the static pressure, we compare this result, where the reference point of the constant static pressure, i.e. constant value of  $\sigma_{ref} = 1.0$ , is located ahead of the hydrofoil in the entrance region, with the opposite situation, where the reference point is downstream near the bottom of the test section, see Fig. 10. Now the cavitating flow remains steady, only a very small attached vapor sheet develops at the suction side which causes a lift decrease of about 16% compared with the single phase flow.

### 3.2.2. Interaction of free surface and cavitation dynamics

To avoid this very strong dependence on the assumption of the reference location with identical absolute values of the static pressure, the cavitation problem is coupled with a free surface flow, where the static pressure is constant above the liquid surface, i.e. independent of the location of the reference point. At first, a steady state cavitating flow develops with a slight increase of the lift of about 2% compared with single phase flow. Figure 13 depicts unsteady cavitating flows with separating vapor clouds similar to Fig. 12. For equal values of  $\sigma_{ref}$  the instantaneous displacement of the free surface reduces the cavitation intensity, i.e. the volume fraction  $\alpha$  and the frequency of the shedded vapor clouds. The significant effects on the lift (Table 1), only dependent on the location of the reference point and for identical values of the static pressure at this point follow directly from the cavitation dynamics inside the test section, i.e. from the interaction of the local vapor production, the convective transport and the resulting reaction of the velocity and pressure field. It emphasizes the importance of appropriate boundary conditions and of the inclusion of the dynamical interaction with the entire test circuit.

Table 1: Time averaged lift and drag (per unit meter span) depending on the cavitation number  $\sigma$ , **reference point above free surface**.

$\sigma$	lift [N]	drag [N]	$f$ [Hz]	$\text{Str} = \frac{f \cdot l_c}{U}$
2.5 *	7200	40	steady	steady
2.5 **	3600	50	steady	steady
0.97 ***	3665	150	steady	steady
0.87	3160	480	5.4	0.0585
0.77	3080	550	5.75	0.062
0.67	2660	580	6.0	0.065
0.57	2750	680	$\sim 9.0$	0.0975

- \* noncavitating **without** free surface
- \*\* noncavitating **with** free surface
- \*\*\* cavitating **with** free surface and equal static pressure at the tip of the hydrofoil as in \*.

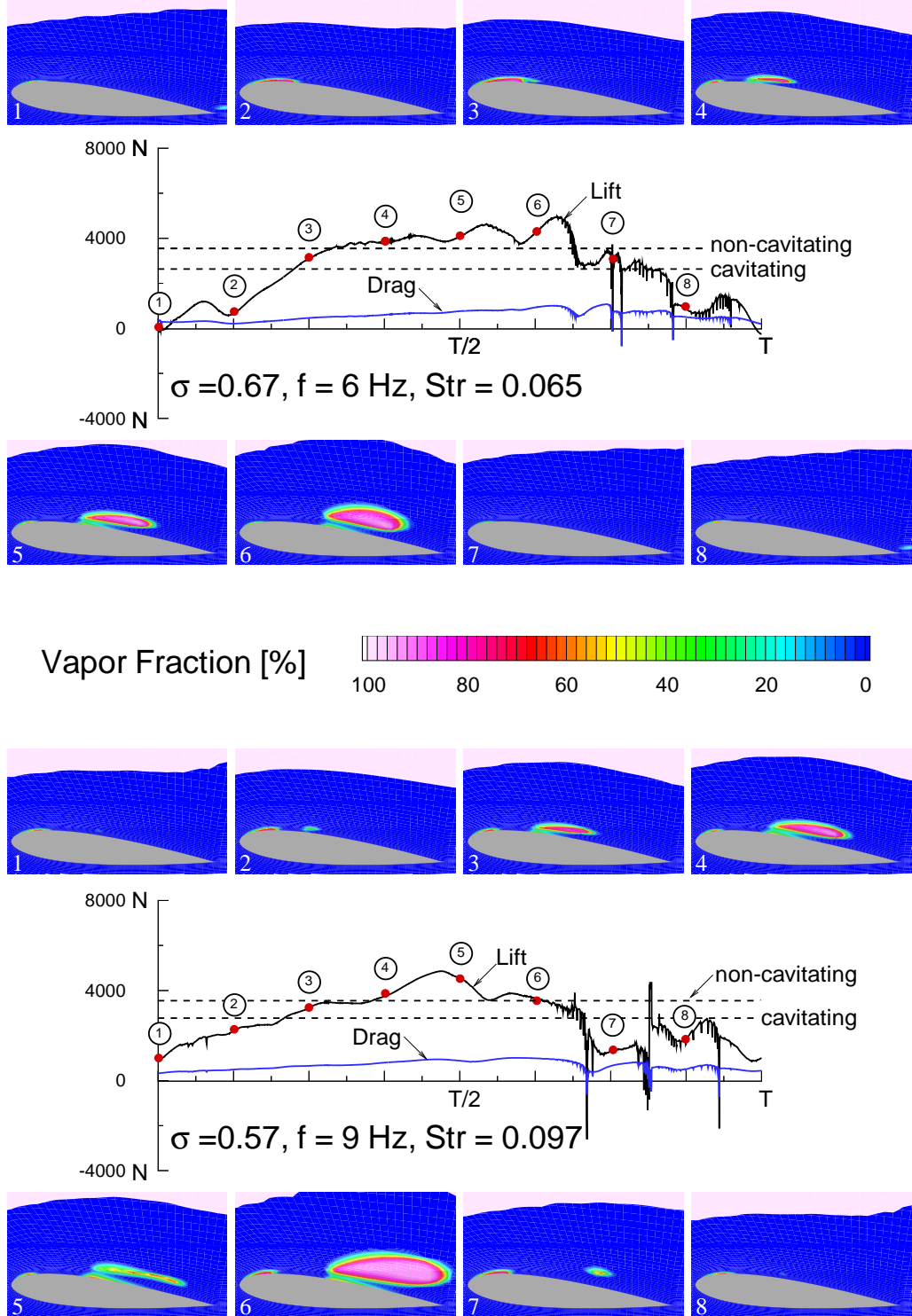


Fig. 13: Unsteady lift, drag and vapor distribution for one cavitation cycle. Time increment:  $\Delta t = T/8$ ,  $l_c = 0.13\text{m}$ ,  $n_0 = 10^8 \text{nuclei/m}^3 \text{water}$ ,  $R_0 = 3.0 \cdot 10^{-5}\text{m}$ , water at 293.15K, **reference point above free surface**.

#### 4. Conclusions

For identical absolute values of the static pressure we observe unsteady shedding vapor clouds or only small steady attached cavities, depending on the location where the static pressure is fixed by  $\sigma_{ref}$ , upstream or downstream of the hydrofoil, respectively. Qualitative and quantitative agreement with experiment is only achieved if the reference point is at the inlet of the test section, i.e. upstream of the

hydrofoil. To avoid the high sensitivity of the resulting two-phase flow to individual boundary conditions we investigate a third configuration with a free liquid surface above the hydrofoil. The free surface removes the stiffness in the physical domain and of the numerical treatment, leading to much faster convergence of the calculation. However, simulations with and without a free surface demonstrate the strong variation of lift and drag caused by unsteady cavitation, which is in good agreement with experiments of Keller and Arndt (1999).

### Acknowledgment

The authors gratefully acknowledge the support from the Deutsche Forschungsgemeinschaft (DFG) during performing this work. Special thanks are given to Prof. Dr.-Ing. M. Perić and Dipl.-Phys. M. Krömer from the TU Hamburg-Harburg for providing the single phase version of the numerical code, and to Dr. rer. nat. A. Keller (TU Munich) and Prof. R.E. Arndt (Univ. Minnesota) for providing experimental data for the NACA 0015 hydrofoil.

### References

- Arndt, R.E., 1981. Cavitation in Fluid Machinery and Hydraulic Structures. In: Ann. Rev. Fluid Mech., Vol. 13, pp. 273-328.
- Brennen, C. E., 1998. Cloud cavitation: Observations, calculations and shock waves. Multiphase Science and Technology, Vol. 10., pp. 303-321.
- Ferziger, J.H., Perić, M., 1996. Computational methods for fluid dynamics. Springer-Verlag.
- Gindroz, B., Billet, M.L., 1976. Influence of the nuclei on the cavitation inception for different types of cavitation on ship propellers. J. of Fluids Engineering, pp. 87-97.
- Keller, A., Arndt, R.A., 1999. Private communication.
- Keller, A., Arndt, R.A., 2000. Cavitation scale effects - a presentation of its visual appearance and empirically found relations. In: Proc. of NCTC50 International Conference on Propeller Cavitation, April 2000, Newcastle upon Tyne.
- Lee, H.S., Merte, H., 1996. Spherical vapor bubble growth in uniformly superheated liquids. Int. Journal of Heat Mass Transfer, Vol. 39, No. 12, pp. 2427-2447.
- Li, C.Y., Ceccio, S.L. Ceccio, 1994. Observations of the interactions of cavitation bubbles with attached cavities. In: ASME-FED Vol. 190, pp. 283-290.
- Nichols, B.D., Hirt, C.W. ,1973. Calculating three-dimensional free surface flows in the vicinity of submerged and exposed structures. Journal of Comp. Physics, Vol. 12, pp. 343-448.
- Plesset, M.S., Prosperetti, A., 1977. Bubble dynamics and cavitation. In: Annual Review of Fluid Mechanics, Vol. 9, pp. 145-185.
- Reboud, J.L., Delannoy Y., 1994. Two-phase flow modeling of unsteady cavitation. In: Proc. 2nd Int. Symp. on Cavitation, Tokyo, Japan.
- Sauer, J., 2000. Instationär kavitzierende Strömungen - Ein neues Modell, basierend auf Front Capturing (VoF) und Blasendynamik. Ph.D. thesis (in German), University of Karlsruhe, Germany.
- Sauer, J., Schnerr, G.H., 2000. Unsteady cavitation dynamics -dependence on modeling and boundary conditions. In: Proc. 2nd Japanese-European Two-Phase Flow Group Meeting, September 25-29, Tsukuba, Japan.
- Sauer, J., Winkler, G., Schnerr, G.H., 2000. Cavitation and condensation - common aspects of physical modelling and numerical approach. Chemical Engineering and Technology, Vol. 23, Nr. 8, pp. 663-665.
- Schnerr, G.H., Adam, S., Lanzenberger, K., Schulz, R., 1995. Multiphase flows: Condensation and cavitation problems. In: Computational Fluid Dynamics REVIEW (eds. M. Hafez and K. Oshima), John Wiley & Sons, Ltd.
- Spalding, D.B., 1974. A method for computing steady and unsteady flows possessing discontinuities of density. CHAM report 910/2.
- Ubbink, O., 1997. Numerical prediction of two fluid systems with sharp interfaces. Ph.D. thesis, University of London.
- Versluis, M., Schmitz, B., von der Heydt, A., Lohse, D., 2000. How snapping shrimp snap: Through cavitating bubbles. In: Science, Volume 289, pp. 2214-2117.
- Winkler, G., Heiler, M., Schnerr, G.H., 1999. Homogeneous/heterogeneous condensation dynamics in turbulent low pressure turbine flows. In: Proc. Int. Conf. SYMCOM99, Cieplne Maszyny Przeplywowe, Turbomachinery, No. 115, Lodz, Polen, pp. 445-456.